

Fabrication of Integrated Ni-Ti Alloys Possessing Both Super-elastic and Shape Memory Properties by Laser Powder Bed Fusion

Jianran Lv (✉ 553876728@qq.com)

Zhejiang University

Hongyao Shen

Zhejiang University

Jianzhong Fu

Zhejiang University

Research Article

Keywords: Integrated Ni-Ti alloys, Super-elastic, Shape memory effect, Laser powder bed fusion

Posted Date: March 8th, 2021

DOI: <https://doi.org/10.21203/rs.3.rs-276783/v1>

License:  This work is licensed under a Creative Commons Attribution 4.0 International License.

[Read Full License](#)

Abstract

Purpose: Integrated Ni-Ti alloys possessing both super-elastic (SE) properties and shape memory effects (SMEs) greatly increase the flexibility of designing complex systems and have broad application prospects. However, existing research mainly focuses on connecting ready-made SE parts and SME parts through welding.

Method: In this paper, laser powder bed fusion (LPBF) was used to fabricate integrated Ni-Ti alloys. First, SE parts with high relative density were fabricated with a Ni-rich powder. Then, different process parameters were used to fabricate the SME parts with a Ti-rich powder based on the SE parts. The integrated component with the best mechanical properties herein was selected. Metallographic analysis, energy dispersive X-ray spectroscopy, differential scanning calorimetry and micro-hardness analyses were carried out for this sample.

Findings: The results show that the integrated component possessed both SE and SME properties at room temperature. Moreover, at the junction of the two materials, the grains were continuous and complete, which indicates that the joint had good quality.

Originality: Our work confirms that LPBF is a feasible method to fabricate integrated Ni-Ti alloys possessing both SE and SME properties.

1. Introduction

Ni-Ti, a shape memory alloy, has been commonly used in many fields due to its excellent super-elastic (SE) and shape memory effect (SME) properties [1–2]. In recent years, much research has been invested in this domain. With an increased understanding of the deformation mechanism of Ni-Ti alloys, their application in the aerospace, automation, medical and other fields should rise [3–8].

The content of Ni in a Ni-Ti alloy greatly affects its transformation temperature and shape memory performance [9]. Normally, when the working temperature of the Ni-Ti alloy is lower than transformation temperature, it will exhibit super-elasticity; otherwise, it will exhibit shape memory effect. The integration of Ni-Ti alloys with different shape memory properties should greatly increase the flexibility for engineering applications [10–13]. Researchers [12] proposed a novel shape memory alloy actuator that contained two different material compositions in one monolithic piece of actuator wire. Among them, one shows the SME for actuation, and the other exhibits SE properties, which are applied to estimate the position. In [13], a robot finger combined with Ni-Ti (SE) and Ni-Ti (SME) wires was produced to exhibit multi-functional structures. Because of the good application prospects of these monolithic structures, we believe that additional applications will be found in the future.

The properties of Ni-Ti, such as high ductility, work hardening, and adhesion, present huge challenges for the machining of Ni-Ti alloys [14–18]. Therefore, the laser welding process is often used as a method of joining Ni-Ti alloys with different material compositions [19]. Mehrshad Mehrpouya et al. found the

optimal laser parameters to join the dissimilar Ni-Ti (SE) to the Ni-Ti (SME) by laser welding and analysed various properties [10]. Zhi Zeng et al. investigated the influence of the welding process parameters on the joint strength, and the properties of the group with the highest joint strength were studied [11]. However, welding also has disadvantages. For example, the welding process substantially affects the properties of the welded region, which may reduce the quality of the connection of the two parts [20–21]. The welding process also makes the welded area rough, which affects the appearance of the monolithic structure [10–11, 20–21]. Moreover, welding of different micro-components is also a relatively difficult task now.

Laser powder bed fusion (LPBF) is a very promising method for fabricating Ni-Ti alloys, and the influence of process parameters on their various properties has been extensively investigated [22–28]. For LPBF, first, the component should be cut into pieces, and then a laser is used to melt and print the component layer by layer until it is completed. This convenient processing method makes it possible to fabricate different material compositions as one component. In terms of fabricating heterogeneous material parts with LPBF, a substantial amount of research has been done, but the materials have usually been Ti, Fe, and stainless steel [29–31]. The monolithic structures of Ni-Ti alloys with different material compositions fabricated with LPBF can prevent certain problems that appear in during welding, such as a rough appearance, and there are also advantages in the fabrication of multifunctional microstructures.

In this paper, LPBF was used to fabricate Ni-Ti alloys that combine both SE and SME properties. The optimal process parameters were used to fabricate the SE part with a high relative density first. The SME parts were then fabricated with process parameters B1 to B6 based on the SE part. The integrated component with the best mechanical properties herein was selected for additional study. The microstructure, fracture morphology, transformation temperature, Ni-Ti ratio and hardness of this sample were studied to show that it was a complete and continuous integrated component that possessed both SE and SME properties. Our work confirmed that LPBF is a feasible method to fabricate integrated Ni-Ti alloys that possess both SE and SME properties.

2. Materials And Methods

Ni₅₄Ti₄₆ (at.%) powder (Ni content measured by Inductively Coupled Plasma(ICP): 59.12(wt.%) powder and Ni₄₆Ti₅₄ alloy (Ni content measured by ICP: 51.21(wt.%) powder were used in this work. The details are shown in Table 1. Figure 1 (a) shows the overall process of the experiment. We first used the Ni₅₄Ti₄₆ powder to fabricate 10 mm×10 mm×15 mm components that exhibited SE properties at room temperature. Then, we replaced the Ni₅₄Ti₄₆ powder with the Ni₄₆Ti₅₄ powder to fabricate components of the same size that exhibited a SME, as shown in Figure 1 (b). A Nd:YAG laser with a 1064 nm wavelength and 80 μm spot size was used to scan and melt the Ni-Ti powder. Table 2 shows the process parameters. According to [24-25], process parameter set A can be used to fabricate SE components with high relative density. The influence of the process parameters on the Ni-rich powder and Ti-rich powder was different. Especially at the junction of the two materials, the required energy density may be unique due to the sudden change in Ni content at the joint. To investigate the effect of the process parameters on the

bonding strength of the two parts, SME parts were fabricated using process parameter sets B1 to B6. The integrated components were then machined into dog-bone shapes, the size of which are displayed in Figure 1 (c). For each combination of process parameters, at least seven samples were made for the tests.

Table 1- Details of powders in this work.

Number	Composition(at.%)	Morphology of the powder	Type of powder
□	Ni ₅₄ Ti ₄₆	spherical	pre-alloyed
□	Ni ₄₆ Ti ₅₄	spherical	pre-alloyed

Table 2- List of process parameters.

Number	Energy density (J ⁻¹ mm ⁻³)	Laser power (w)	Scanning velocity (mms ⁻¹)	Hatch spacing (mm)	Layer thickness (mm)
A	150	150	250	0.08	0.05
B1	93	150	400	0.08	0.05
B2	107	150	350	0.08	0.05
B3	125	150	300	0.08	0.05
B4	150	150	250	0.08	0.05
B5	187.5	150	200	0.08	0.05
B6	250	150	100	0.08	0.05

To investigate the maximum ultimate tensile strength (UTS), tensile tests were conducted using a universal testing machine (UTM2203, Suns Technology Stock Corp., Shenzhen, China) at a stretching rate of 10 mm/min. The sample with the highest UTS herein was selected for subsequent tests. A metallographic microscope (METALLUX-II, Leitz Wetzlar, Germany) was employed to perform metallographic analysis. Scanning electron microscopy (SEM, Quanta 450 FEG, America) was used to study the fracture morphologies and micro-morphologies. Before carrying out metallographic microscopy and SEM analyses, the samples were ground, polished, and then etched with a mixed solution of HF:HNO₃:H₂O = 1:5:10. The Ni/Ti ratio was evaluated by energy dispersive spectroscopy (EDS). The micro-hardness was measured using a Vickers micro-hardness tester (HVS-1000). Differential scanning calorimetry (DSC, METTLER TOLEDO Group, Switzerland) was performed to measure the transformation temperatures of the samples with a heating and cooling rate of 10°C/min.

3. Results And Discussion

3.1 Tensile test

Figure 2 (a) exhibits the fracture sites from each sample. As shown in Fig. 2 (a), samples A-B1 to A-B4 all broke at the junction of the two materials, and their corresponding UTS increased. A-B5 and A-B6 broke at the SE part. The UTS of A-B5 and A-B6 were not substantially different and reached the highest value compared to that of the other four groups. However, their UTS values are still slightly lower than the components fabricated by a single kind of material (417.22 MPa for SE component and 410.88 MPa for SME component).

For sample A-B1 to sample A-B4, since low energy densities were used to fabricate the SME part of these samples, the bonding between adjacent layers was insufficient, and there were many defects (such as pores and microcracks) in the SME part. The effect of the low energy density on the bond strength at the junction of the two materials was very obvious. Since the SE part comprised austenite at room temperature while the SME part comprised martensite, the low energy density resulted in a lower bond strength at the junction of the two materials than that of the other parts so that samples A-B1 to A-B4 all broke at the junction.

As the energy density during fabrication of the SME part increased, the density of the SME part also increased, and the bonding strength at the junction of the two materials greatly improved so that the two parts were regarded as integrated. As shown in Fig. 2 (a), A-B5 and A-B6 all broke in the SE part. We infer that this was caused by the different properties of the SE part and SME part. Figure 3 shows the stress-strain curves of the SE, SME and A-B5 parts. The UTS of A and B are very close. However, compared with that for the SE part, the SME part had better ductility and underwent plastic deformation during stretching. A-B5 contained both the SE part and SME part. The trend of the stress-strain curve for A-B5 is similar to that of the SME part, which indicates that A-B5 also underwent plastic deformation during stretching due to the SME part. Nevertheless, due to the existence of the SE part, the ductility of A-B5 was slightly worse than that of the SME part. The brittleness of the SE part was greater than that of the SME part, so A-B5 and A-B6 fractured at the SE part.

The fabrication of components using an excessively high energy density results in the formation of excessive impurities and Ni evaporation in the final selective laser melted samples. Therefore, on the premise of ensuring that the integrated components have a high relative density and good joint quality, the energy density for fabricating the SME part should be as low as possible. Here, A-B5 was selected for further study.

Figure 4 (a) and (b) shows the fracture morphology of A-B1 and A-B5, respectively. Since B1 was fabricated with a low energy density, many unmelted powder particles were found on the fracture surface at the junction of the two materials, as shown in Fig. 4 (a), which was regarded as the site for fracture initiation. The large smooth surface area caused by the unmelted powder demonstrated a brittle fracture

mechanism. Moreover, there was also a small rough surface area shown in Fig. 4 (a-1), indicating the presence of plastic deformation during the fracture process.

In comparison to the fracture surface of A-B1, the rough surface occupied most of the fracture surface of A-B5, as shown in Fig. 4 (b). Figure 4 (b-1) shows a magnified view of the fracture surface of A-B5. The river-shaped stripes were tearing edges produced during the fracture process, implying the presence of quasi-cleavage fracture. Defects, such as microcracks and pores, generated during the LPBF process produced cleavage cracks during the stretching process, expanded into planes, and finally tore in a plastic manner. Figure 4 (b-2) shows the small and shallow dimples on the tearing edges, confirming that plastic deformation occurred during the stretching process.

3.2 Metallographic analysis

Figure 5 shows a metallographic image of A-B5 after being ground, polished, and etched. Because the corrosive had different effects on the SE part and SME part, the metallographic image was clearly divided into two parts. Although A-B5 had a high relative density (98.3% of 6.45 g/cm³), Fig. 5 shows that there were still a few defects, such as micro-cracks and pores, in the integrated component. Brittle intermetallics generated during LPBF were the main reason for these defects [24]. The grains in the SE part and SME part in the building orientation were both elongated columnar crystals. Although there was a sudden change in colour at the joint, we found that there were continuous grains. That is, at the joint, the grains were complete and not cut off, confirming the good quality at the joint.

Figure-reference is quoted from [10] which shows the integrated Ni-Ti alloys fabricated by welding. Welded integrated Ni-Ti alloys can be divided into 3 regions: base material, heat-affected zone and fusion zone. According to reference [10], the defected and cracks produced by welding basically appear in the fusion zone. We can also observe from figure-reference (c) that the region occupied by fusion zone is relatively large which has negative effects on the performance of the component. Compared with welded integrated Ni-Ti alloy, LPBFed integrated Ni-Ti alloy doesn't have these three regions but instead a continuous whole, which displays better quality on the joint.

3.3 SEM analysis

Figure 6 shows the SEM image of sample A-B5. The integrated component acts like a whole and there is no obvious sign of connection at the joint. Due to the high Ni content in the powder used to fabricate SE part, Ni-rich precipitation is likely to occur during the process. Ni-rich intermetallics were found on the surface of SE part. In the SME part, Ti oxides and Ti-rich phases are more likely to be generated since the powder has higher Ti content and we found Ti oxides on the surface on the SME part. During the manufacturing process, these intermetallics and oxides will be mixed between the layers, so that the connection area between the layers will be reduced, and eventually lead to the generation of the micro-cracks. Meanwhile, these intermetallics and oxides can also cause local variations of Ni/Ti ratio, leading to local fluctuations in the local hardness and transformation temperatures which will be discussed in the following article.

3.4 EDS analysis and micro-hardness analysis

EDS and micro-hardness analyses were carried out for A-B5. Starting from the centre point, micro-hardness and EDS measurements were performed at intervals of 0.1 mm along both sides. Figure 7 (a) shows the results of the EDS measurement. On the SE side, the Ni content fluctuated around 52.5%. As a large amount of Ni was evaporated during processing, the Ni content of the SE part was very reduced compared to that for the powder that was used to fabricate the SE part. However, the proportion of Ni content was approximately 47% on the SME side, which is slightly higher than that in the $\text{Ni}_{46}\text{Ti}_{54}$ powder since the evaporation of Ti was greater than the evaporation of Ni on the SME side. There was a sudden change in Ni content at the junction of the two materials. The length of the area where the Ni content changed ranged from approximately 0.1 mm to 0.2 mm. Compared to those in integrated components connected by welding that usually have fusion zones whose lengths are more than 1 mm and always break at the junction of the two materials during tensile tests [10, 11], the integrated components fabricated by LPBF had narrower anomalous areas and possessed better quality at the joint. Figure 7 (b) shows the results of micro-hardness measurements. It is well known that Ni-Ti alloys with a high percentage of Ni have a high hardness so that the SE side was harder than the SME side, as shown in Fig. 7 (b)[10]. Furthermore, we found that the hardness also had a sudden change at the junction of the two materials, indicating that the properties of the material in this area changed. The above results all show that the integrated component was clearly divided into two parts and had a narrow anomalous area and good quality at the joint.

3.5 DSC test

As shown in Fig. 8 (a), we divided A-B5 into two parts, the SE part and the SME part, and then performed DSC tests on these two parts. Figure 8 (b) shows the results. The transformation temperature curve of the SME part had a narrow and sharp transformation temperature peak. However, the SE part had a broad and flat transformation peak, which was ascribed to the large amount of Ni-rich precipitates and impurities generated during the LPBF process. During the thermal cycle, since the thermal expansion coefficient of these second particles is different from that of the matrix, thermal mismatch strain will generate at the interface between the particles and the matrix. The mismatch strain can further cause lattice distortion and stress field which promote phase transformation and reduce the energy required. Therefore the phase transformation occurs earlier. In the other hand, with the progress of the phase transformation, the matrix and particles coordinate with each other and the lattice distortion and stress field gradually decrease.

For the SE part, the austenite start temperature (A_s), austenite finish temperature (A_f), martensite start temperature (M_s) and martensite finish temperature (M_f) were -40°C , 0°C , 20°C , and -60°C , respectively. The A_s , A_f , M_s and M_f of the SME part were 60°C , 95°C , 60°C and 12°C , respectively. Therefore, at room temperature, the SE part usually comprised austenite and exhibited superelasticity, while the SME part comprised martensite and possessed a shape memory effect so that the integrated components demonstrated two functions at the same time.

4. Conclusion

In this paper, LPBF was used to fabricate integrated Ni-Ti alloys that combined a SE part and SME part. Process parameter set A was used to fabricate the SE part with a high relative density. The SME parts were fabricated with process parameter sets B1 to B6 based on the SE part. Tensile tests were carried out for integrated components A-B1 to A-B6. As the energy density increased, the UTS of the samples first increased (A-B1 to A-B6) and then remained at the highest value (A-B5 and A-B6). A low energy density resulted in a low bond strength between the layers, especially at the junction of the two materials, so that components A-B1 to A-B4 all broke at the joint. Components A-B5 and A-B6 all broke at the SE part since the SE part had poor ductility and greater brittleness compared with those of the SME part. The brittle fracture caused by the unmelted powder was the main fracture mechanism for A-B1 to A-B4, while quasi-cleavage fracture with plastic deformation was the main fracture mechanism for A-B5 and A-B6. Specimen A-B5 was selected for additional tests. Along the building orientation, the grains of the SE part and SME part were both elongated columnar crystals, and at the joint, the grains were complete and continuous, which confirmed the good quality at this location. The EDS and micro-hardness measurements confirmed that the integrated component was clearly divided into two parts and had a narrow anomalous area where the micro-hardness and Ni content suddenly changed. The DSC test shows that the SE part comprised austenite at room temperature, while the SME part comprised martensite, so they exhibited SE and SME, respectively. Our work confirmed that LPBF is a feasible method to fabricate complete and continuous integrated Ni-Ti alloys possessing both SE and SME.

Declarations

-Ethical Approval and Consent to Participate:

This article does not involve any animal or human experiments.

-Consent to Publish:

Not applicable.

-Authors Contributions:

Lv Jianran mainly finished the experiments and paper writing. Shen and Fu took part in the experiments and guided Lv.

-Funding

This work was financially supported by the National Nature Science Foundation of China (No. 51975518, 51805477), the Science Fund for Creative Research Groups of National Natural Science Foundation of China (No. 51821093), Ningbo Science and Technology Plan Project (2019B10072), and the Fundamental Research Funds for the Central Universities (No. 2019QNA4004).

-Competing Interests

The authors declare that they have no competing interests

-Availability of data and materials

The datasets used or analyzed during the current study are available from the corresponding author on reasonable request.

Acknowledgements

This work was financially supported by the National Nature Science Foundation of China (No. 51975518, 51805477), the Science Fund for Creative Research Groups of National Natural Science Foundation of China (No. 51821093), Ningbo Science and Technology Plan Project (2019B10072), and the Fundamental Research Funds for the Central Universities (No. 2019QNA4004).

References

- [1] Otsuka K, Ren X. Physical metallurgy of Ti–Ni-based shape memory alloys[J]. *Progress in materials science*, 2005, 50(5): 511-678.
- [2] Shape memory and superelastic alloys: technologies and applications[M]. Woodhead Publishing, 2011.
- [3] Mohd Jani J, Leary M, Subic A and Gibson M A 2014 A review of shape memory alloy research, applications and opportunities *Mater. Des.* 56 1078–113
- [4] Elahinia M, Hashemi M, Tabesh M and Bhaduri S B 2012 Manufacturing and processing of NiTi implants: a review *Prog. Mater. Sci.* 57 911–46
- [5] Duerig T, Pelton A and Stöckel D 1999 An overview of nitinol medical applications *Mater. Sci. Eng. A* 15 149–60
- [6] Braz Fernandes F M, Oliveira J P, Machado A and Schell N XRD study of NiTi endodontic files using synchrotron radiation *J. Mater. Eng. Perform.* 23 2477–81
- [7] McDonald Schetky L 1991 Shape memory alloy applications in space systems *Mater. Des.* 12 29–32
- [8] Stoeckel D 1990 Shape memory actuators for automotive applications *Mater. Des.* 11 302–7
- [9] Frenzel J, George E P, Dlouhy A, et al. Influence of Ni on martensitic phase transformations in NiTi shape memory alloys[J]. *Acta Materialia*, 2010, 58(9): 3444-3458.
- [10] Mehrpouya M, Gisario A, Broggiato G B, et al. Effect of welding parameters on functionality of dissimilar laser-welded NiTi superelastic (SE) to shape memory effect (SME) wires[J]. *The International*

Journal of Advanced Manufacturing Technology, 2019, 103(1): 1593-1601.

[11] Zeng Z, Yang M, Oliveira J P, et al. Laser welding of NiTi shape memory alloy wires and tubes for multi-functional design applications[J]. Smart Materials and Structures, 2016, 25(8).

[12]. Zamani N, Khamesee MB, Khan MI (2017) Novel laser processed shape memory alloy actuator design with an embedded strain gauge sensor using dual resistance measurements. Part I: Fabrication and model-based position estimation. Sensors Actuators A Phys 263:234–245

[13]. Engeberg ED, Dilibal S, Vatani M, Choi JW, Lavery J (2015) Anthropomorphic finger antagonistically actuated by SMA plates, Bioinspir Biomim 10(5):056002

[14] Stoeckel D. Forming of nitinol—a challenge[J]. New Developments in Forging Technolog, 2001: 119-134.

[15] Wu S K, Lin H C, Chen C C. A study on the machinability of a Ti49. 6Ni50. 4 shape memory alloy[J]. Materials Letters, 1999, 40(1): 27-32.

[16] Biermann D, Kahleyss F, Krebs E, et al. A study on micro-machining technology for the machining of NiTi: five-axis micro-milling and micro deep-hole drilling[J]. Journal of materials engineering and performance, 2011, 20(4-5): 745-751.

[17] Bellouard Y. Shape memory alloys for microsystems: A review from a material research perspective[J]. Materials Science and Engineering: A, 2008, 481: 582-589.

[18]. Mehrpouya M, Shahedin AM, Daood Salman Dawood S, Kamal Ariffin A (2017) An investigation on the optimum machinability of NiTi based shape memory alloy. Mater Manuf Process 32(13): 1497–1504

[19]. MehrpouyaM, Gisario A, ElahiniaM(2018) Laser welding of NiTi shape memory alloy: a review. J Manuf Process 2018(31):162–186

[20] Tam B, Khan M and Zhou Y 2011 Mechanical and functional properties of laser-welded Ti-55.8 Wt Pct Ni nitinol wires Metall. Mater. Trans. A 42 2166–75

[21] Falvo A, Furgiuele F M and Maletta C 2005 Laser welding of a NiTi alloy: mechanical and shape memory behaviour Mater. Sci. Eng. A 412 235–40

[22] Bormann T, Schumacher R, Müller B, et al. Tailoring selective laser melting process parameters for NiTi implants[J]. Journal of Materials Engineering and Performance, 2012, 21(12): 2519-2524.

[23] Wang X, Kustov S, Van Humbeeck J. A short review on the microstructure, transformation behavior and functional properties of NiTi shape memory alloys fabricated by selective laser melting[J]. Materials, 2018, 11(9): 1683.

- [24] Dadbakhsh S, Speirs M, Kruth J P, et al. Effect of SLM parameters on transformation temperatures of shape memory nickel titanium parts[J]. *Advanced Engineering Materials*, 2014, 16(9): 1140-1146.
- [25] Haberland C, Elahinia M, Walker J M, et al. On the development of high quality NiTi shape memory and pseudoelastic parts by additive manufacturing[J]. *Smart materials and structures*, 2014, 23(10): 104002.
- [26] Bormann T, Müller B, Schinhammer M, et al. Microstructure of selective laser melted nickel–titanium[J]. *Materials characterization*, 2014, 94: 189-202.
- [27] Khoo Z X, Liu Y, An J, et al. A review of selective laser melted NiTi shape memory alloy[J]. *Materials*, 2018, 11(4): 519.
- [28] Elahinia M, Moghaddam N S, Andani M T, et al. Fabrication of NiTi through additive manufacturing: A review[J]. *Progress in Materials Science*, 2016, 83: 630-663.
- [29] Nguyen D, Park H, Lee C, et al. Applying Selective Laser Melting to Join Al and Fe: An Investigation of Dissimilar Materials[J]. *Applied Sciences*, 2019, 9(15).
- [30] Qian T, Liu D, Tian X, et al. Microstructure of TA2/TA15 graded structural material by laser additive manufacturing process[J]. *Transactions of Nonferrous Metals Society of China*, 2014, 24(9): 2729-2736
- [31] Demir A G, Previtali B. Multi-material selective laser melting of Fe/Al-12Si components[J]. *Manufacturing letters*, 2017: 8-11.

Figures

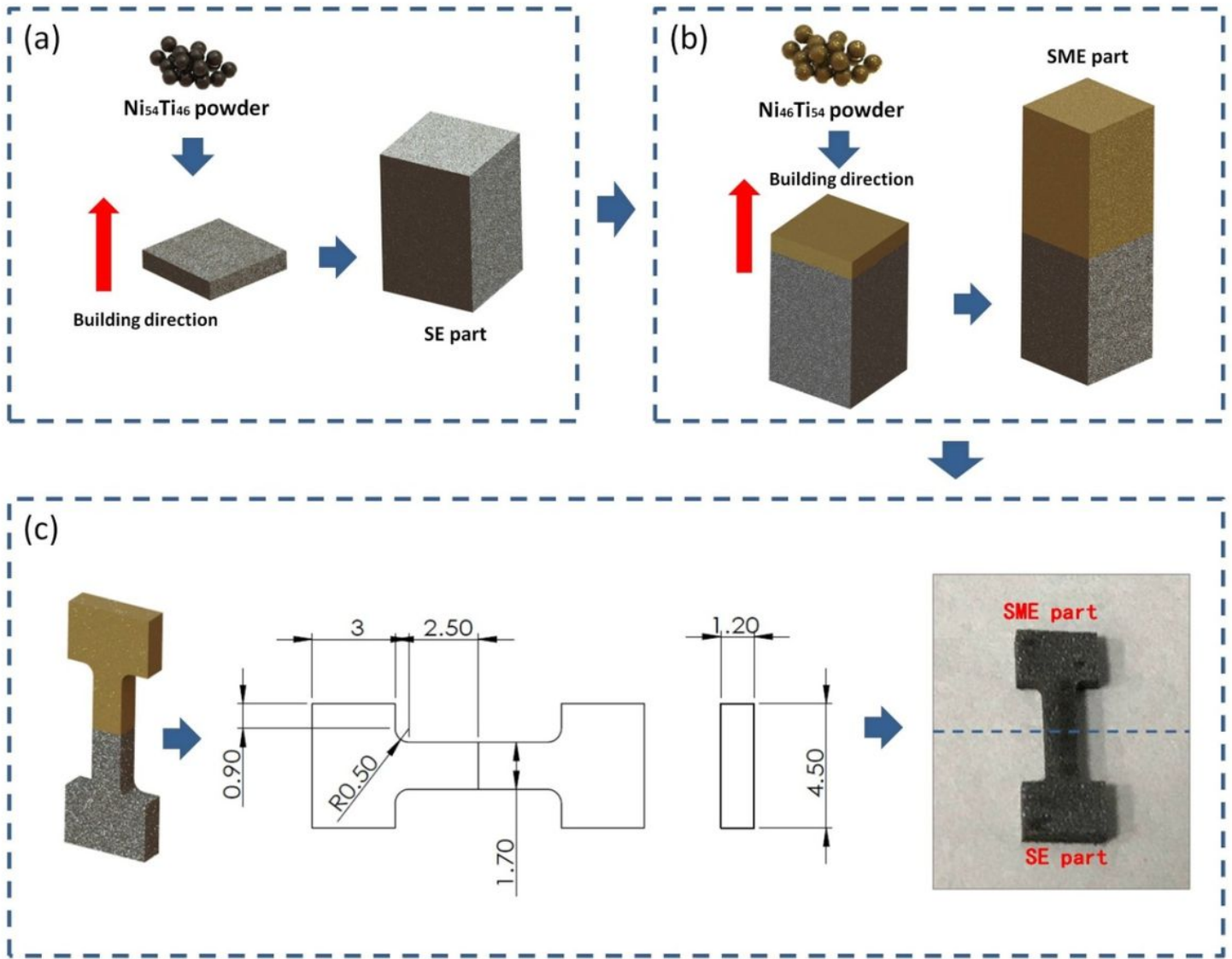


Figure 1

Overall process of the experiment (a) fabricating SE part with $\text{Ni}_{54}\text{Ti}_{46}$ powder (b) fabricating SME part with $\text{Ni}_{46}\text{Ti}_{54}$ powder (c) dog-bone shape specimen and its dimensions

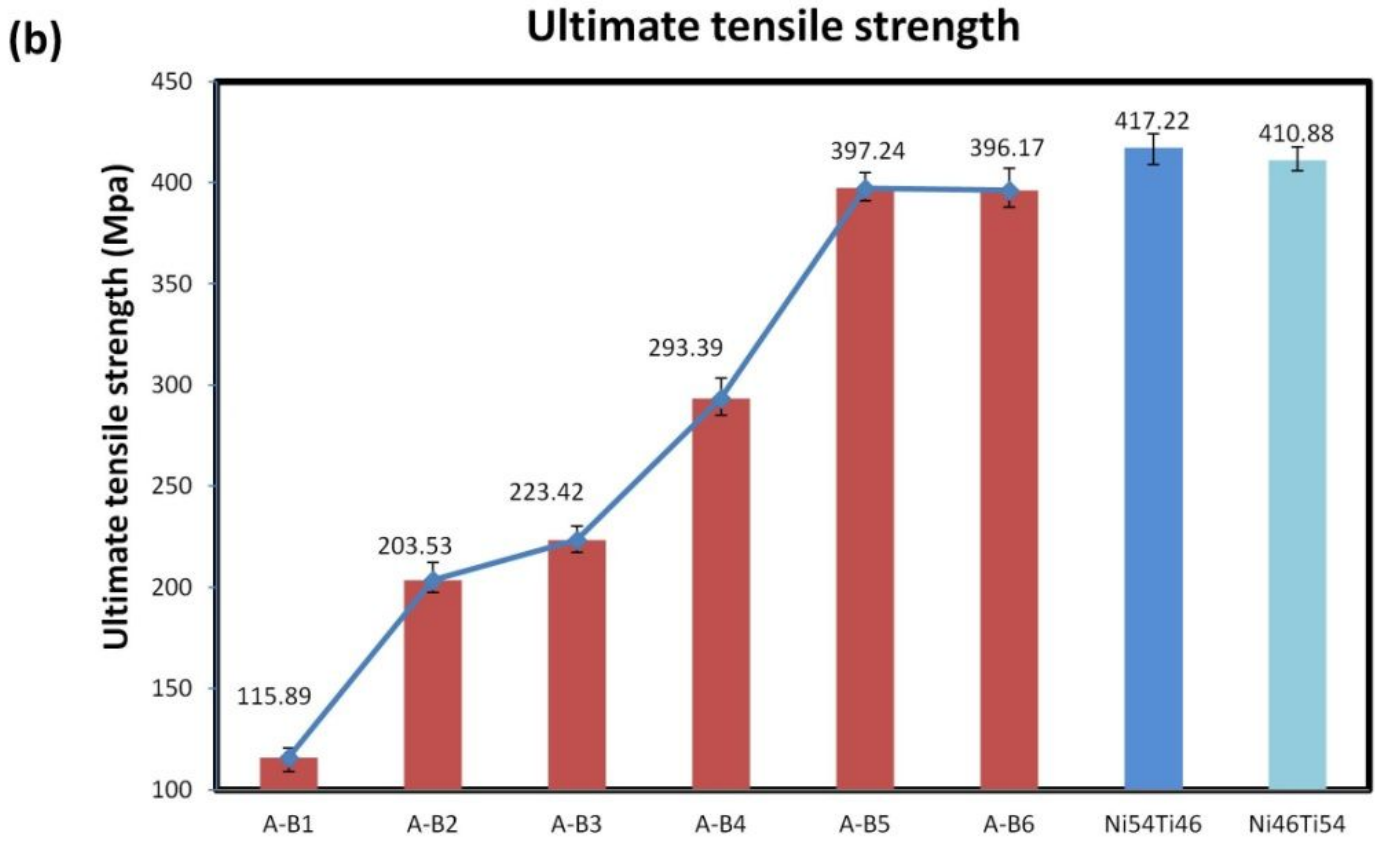
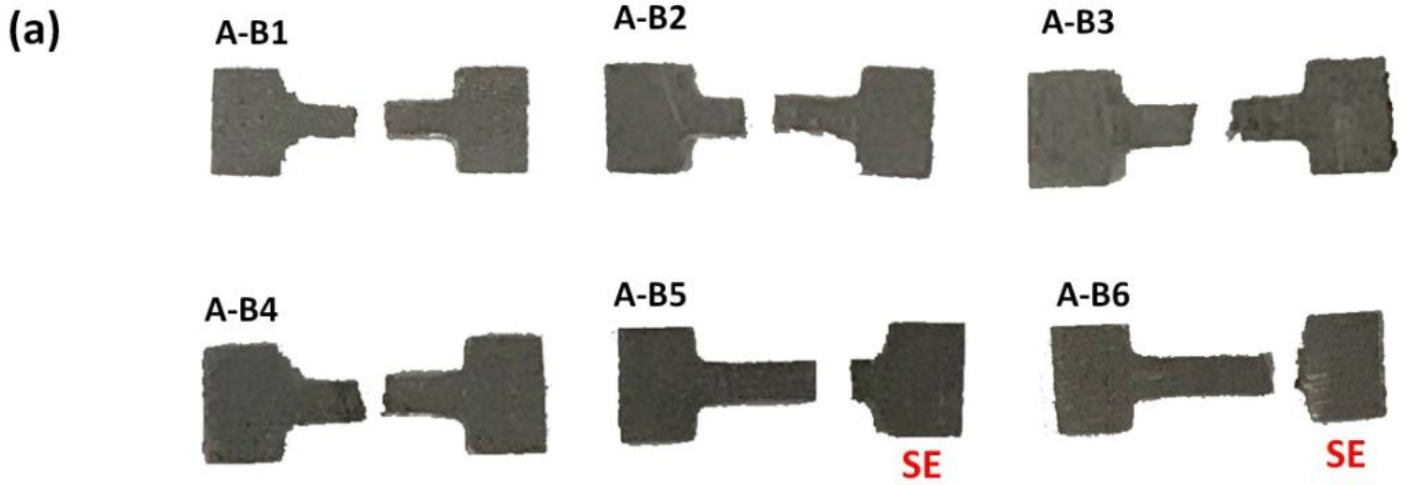


Figure 2

(a) Schematic of fracture site from each sample (b) UTS of each sample

Stress-strain curves

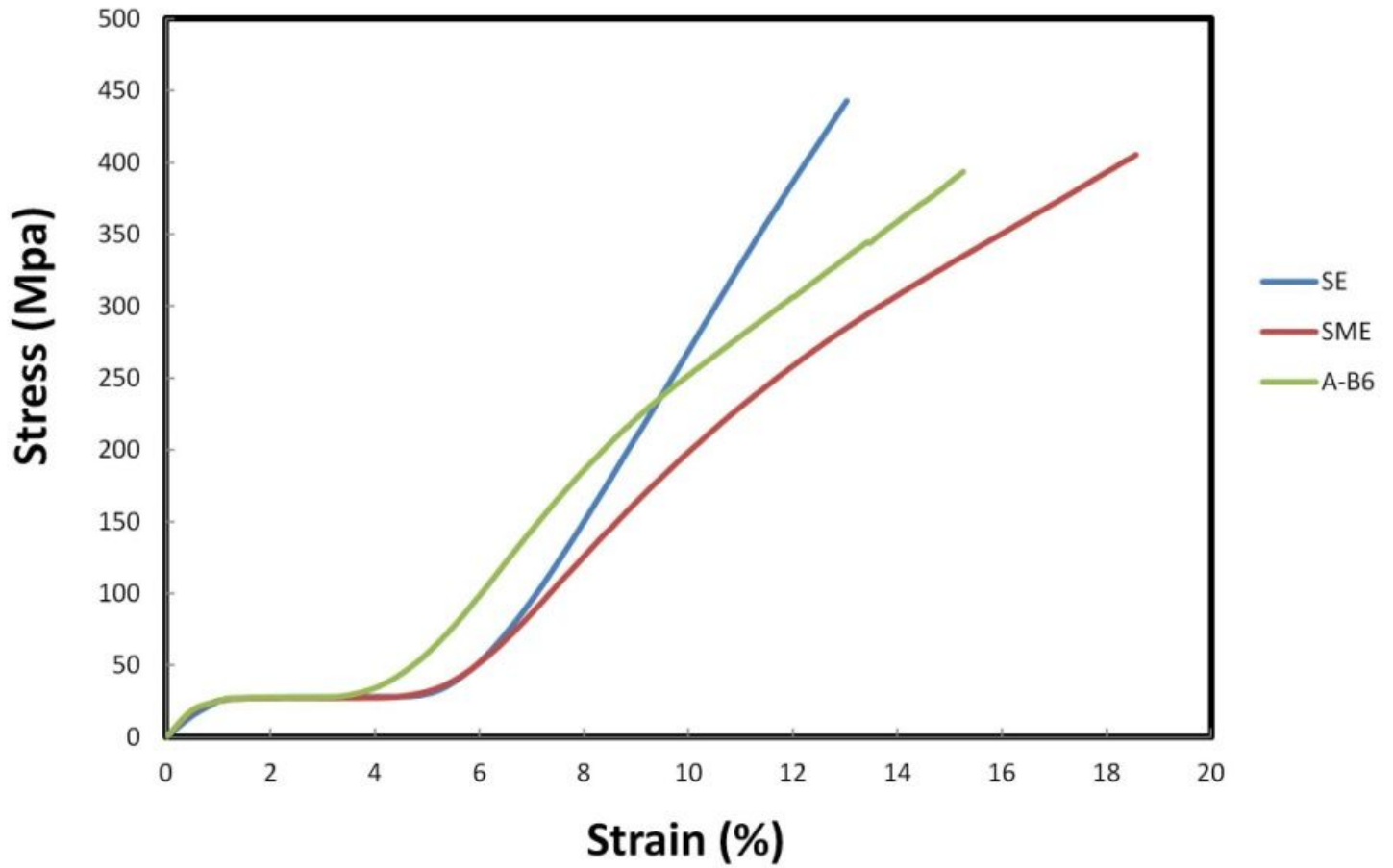


Figure 3

Stress-strain curves of SE component, SME component and A-B5

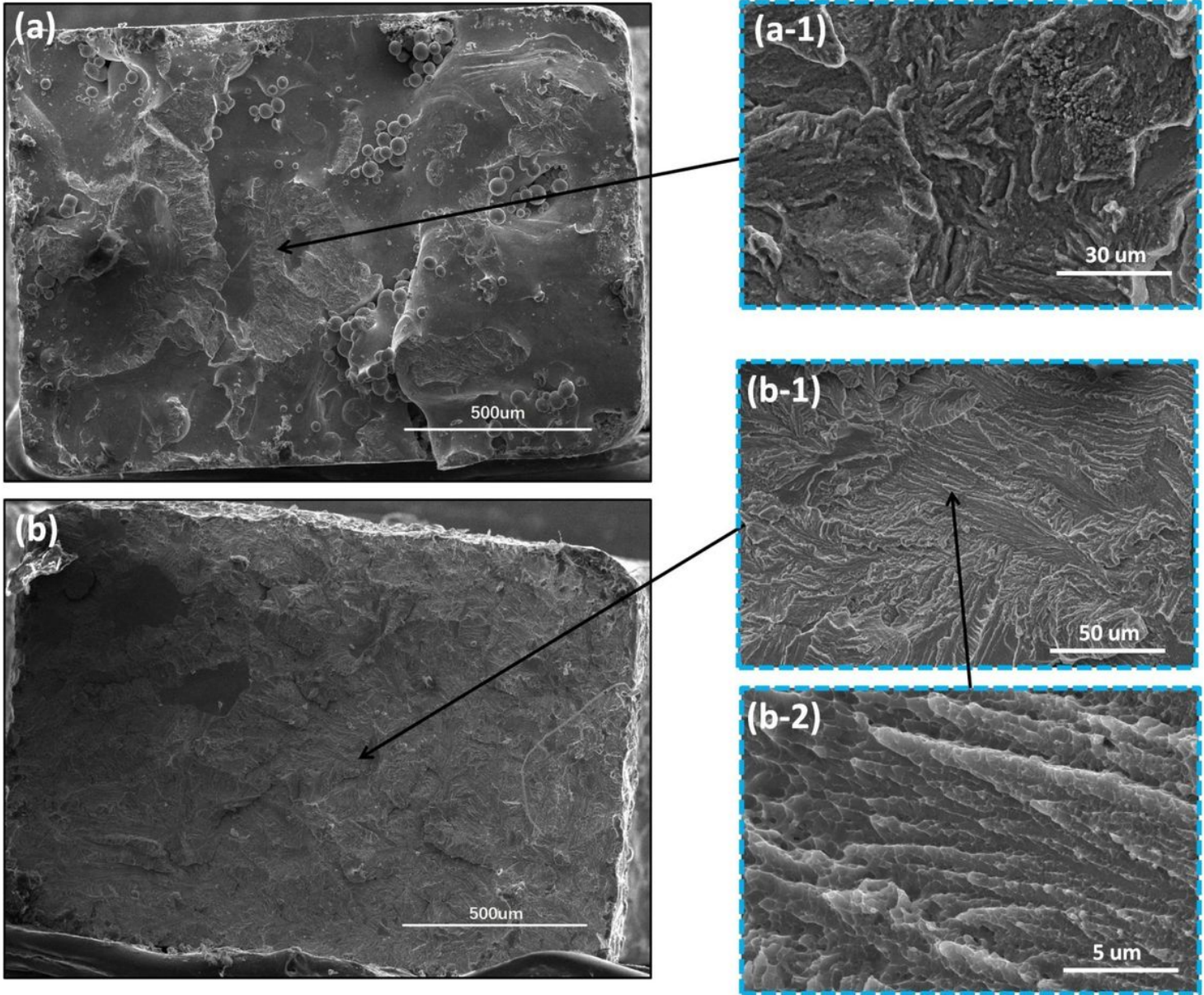


Figure 4

(a) Fracture morphology of A-B1 (b) fracture morphology of A-B5

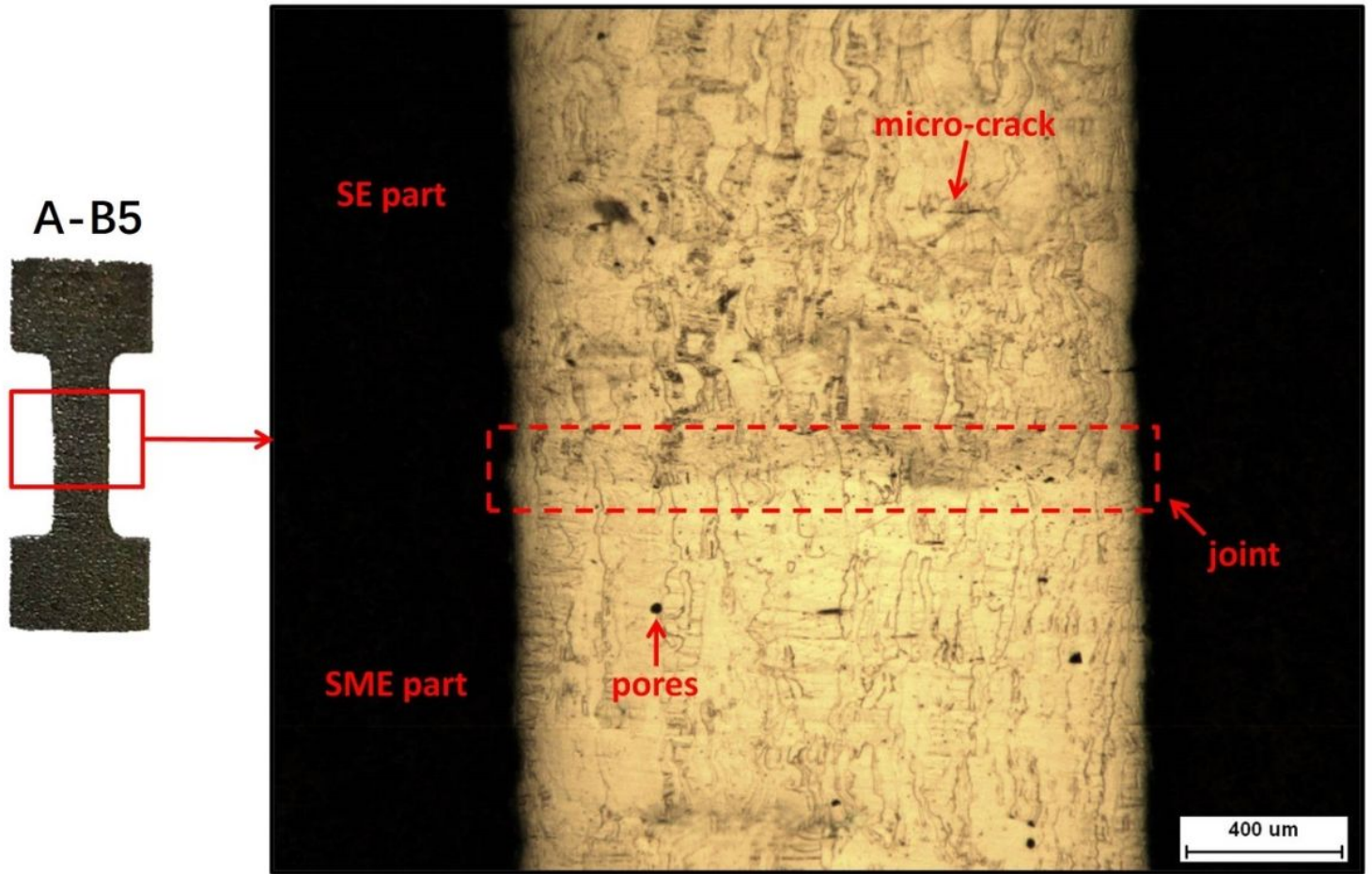


Figure 5

Metallographic diagram of A-B5

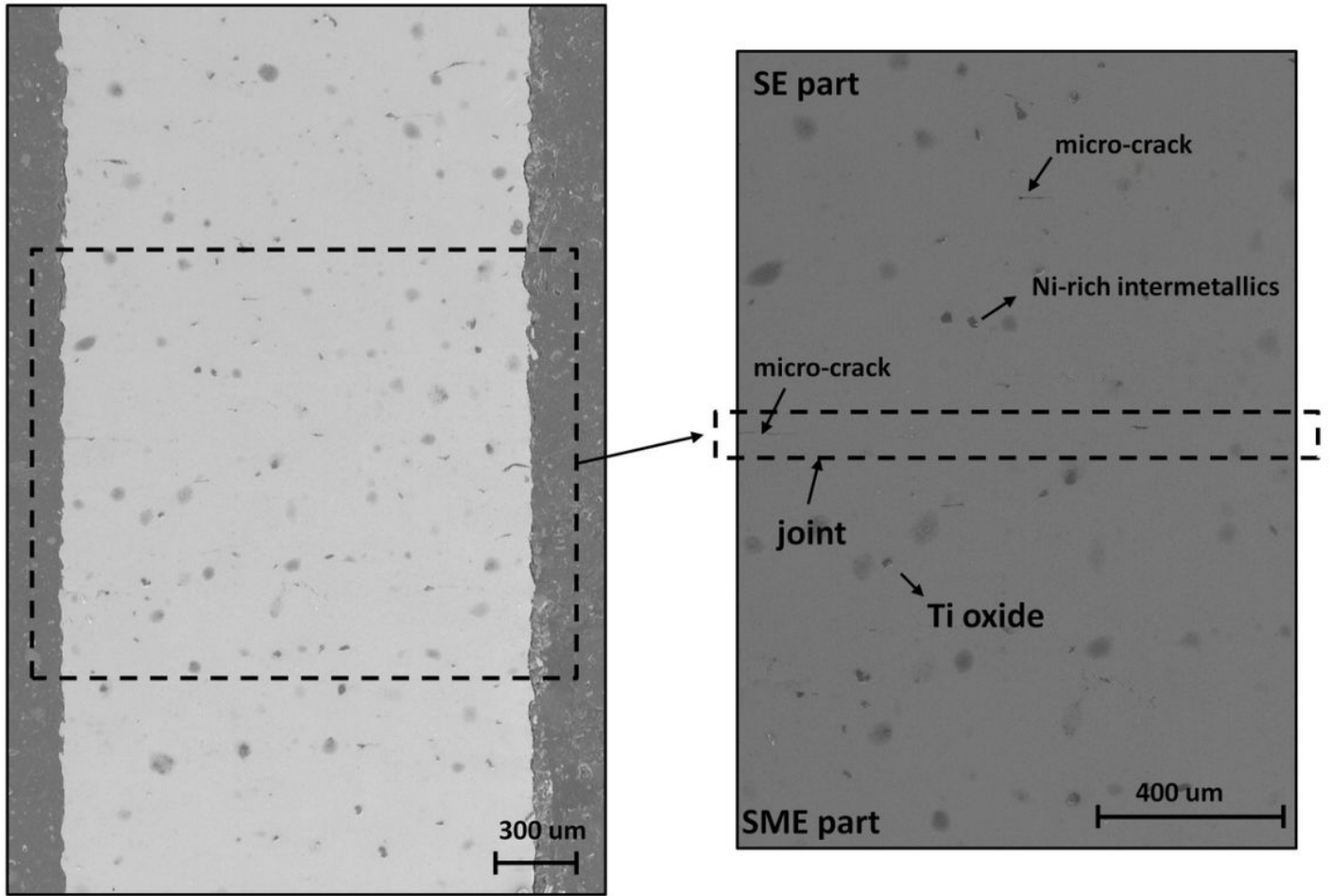


Figure 6

SEM diagram of A-B5

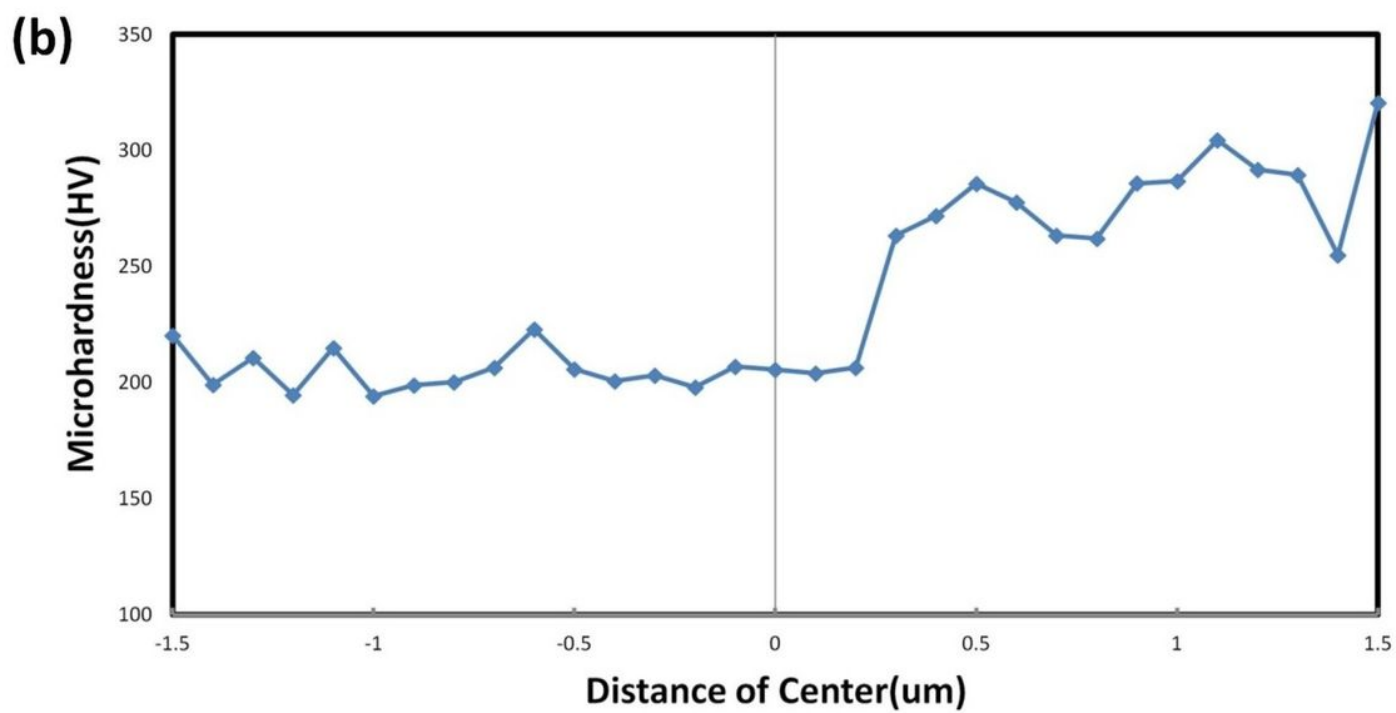
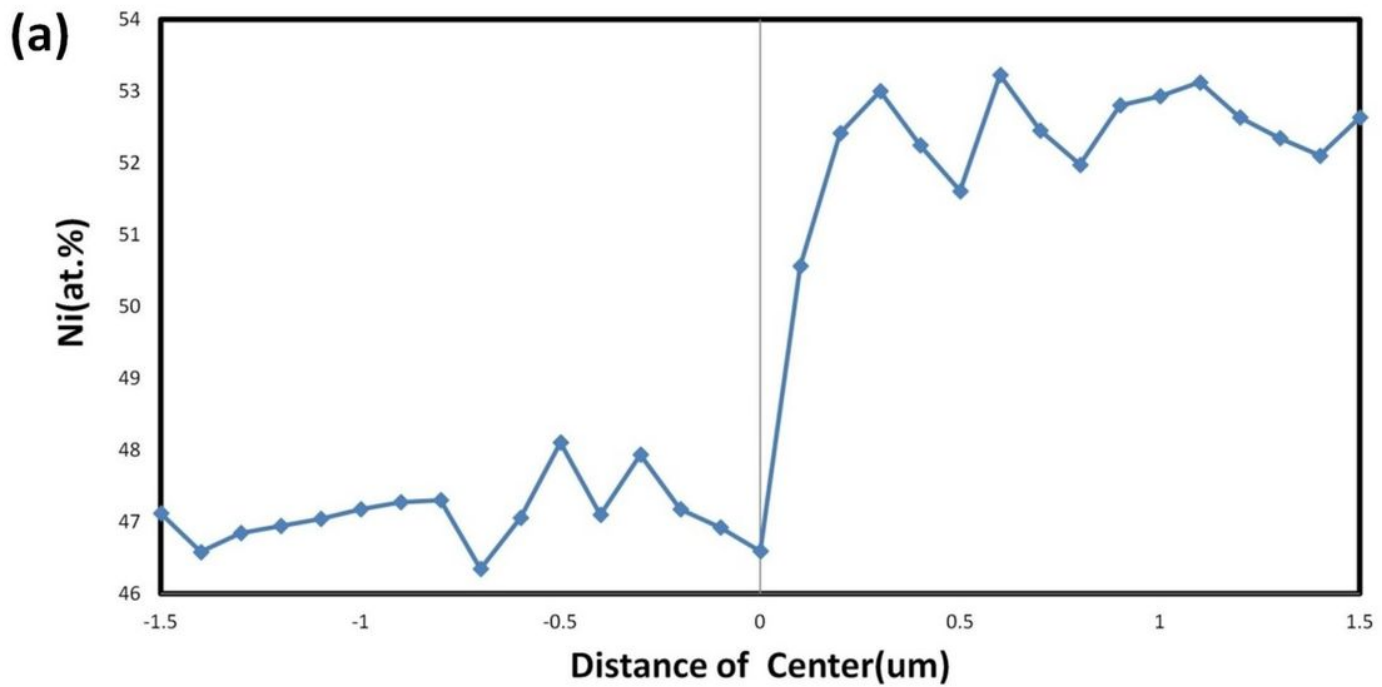
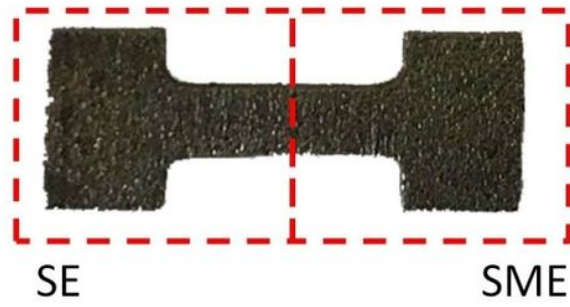


Figure 7

(a) Result of the EDS test for A-B5 (b) result of the micro-hardness test of for A-B5

(a)



(b)

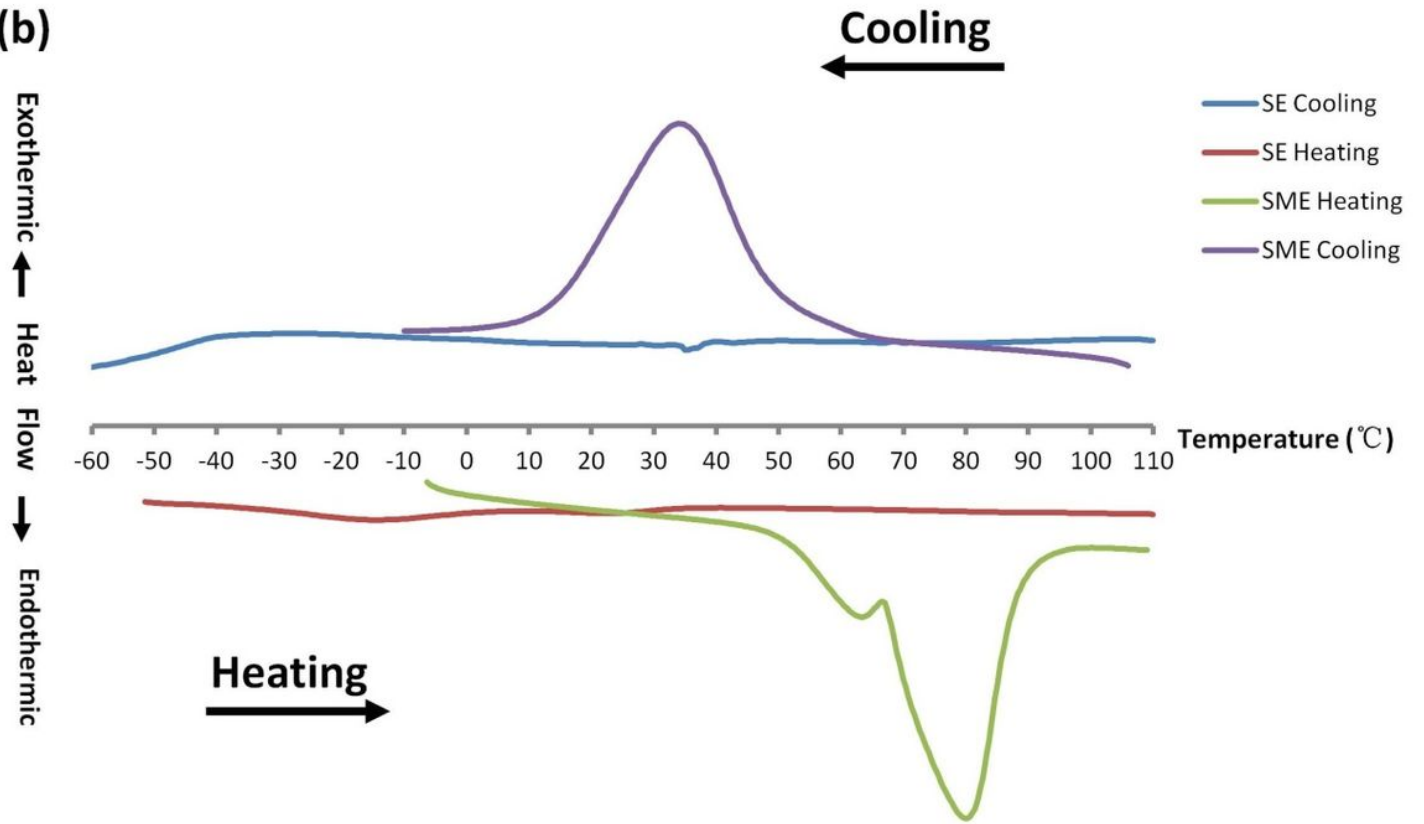


Figure 8

(a) Dividing A-B5 into two parts (b) result of DSC test for A-B5